Magnetic reconstruction of nonaxisymmetric quasi-single-helicity configurations in the Madison Symmetric Torus

Magnetic reconstruction of nonaxisymmetric quasi-single-helicity configurations in the Madison Symmetric Torus

F Auriemma, P Zanca, W F Bergerson[1]**, B E Chapman**[2]**, W X Ding**[1]**, D L Brower**[1]**, P Franz, P Innocente, R Lorenzini, B Momo and D Terranova**

Consorzio RFX, Associazione EURATOM-ENEA sulla Fusione 35127 Padova, Italy
[1] Department of Physics and Astronomy, University of California, Los Angeles, CA 90095, USA
[2] Department of Physics, University of Wisconsin, Madison, WI 53706, USA

Abstract

Quasi-single-helicity (QSH) states, characterized by a magnetic spectrum dominated by the innermost resonant tearing mode, are common to all the reversed field pinch (RFP) experiments. The internal magnetic field structure produced by the dominant mode is investigated for the QSH observed in the Madison Symmetric Torus (MST) RFP in discharges with zero toroidal magnetic field at the plasma boundary. The reconstruction is based on an MHD model coupled to edge measurements of the magnetic field. The model discards pressure, which has little effect on the equilibrium magnetic profile of present RFP plasmas, but adopts a realistic toroidal geometry. The technique is the adaptation to the MST configuration of a procedure already applied in RFX-mod, but a more general radial profile for the current density is needed for an adequate reconstruction of the MST case. The emerging features are similar to those found in RFX-mod. The helical flux surfaces of the dominant mode provide, with a good degree of reliability, a basis for mapping kinetic quantities such as electron density and soft-x-ray emissivity.

(Some figures in this article are in colour only in the electronic version)

1. Introduction

The reversed field pinch (RFP) magnetic configuration is sustained against resistive diffusion due to the dynamo mechanism, a nonlinear process arising from the correlation of the perturbations of the magnetic field with those of the velocity field (MHD dynamo) and the current density (Hall dynamo) [1–3]. The perturbations are produced by MHD resistive-kink/tearing modes [4, 5], mainly with poloidal mode number $m = 1$ and resonant inside the

toroidal field reversal surface, across which this component changes sign [6]. The dynamo appears in two fashions. The first occurs when the perturbation energy is split among many $m = 1$ modes with different toroidal mode numbers n. This magnetic configuration is named the multiple-helicity (MH) state. The second, predicted theoretically and dubbed single-helicity (SH) [7], occurs when the energy is channeled to the innermost resonant tearing mode (dominant mode), leaving the other modes (secondary modes) with negligible amplitude. The closest experimental approximation to SH thus far is quasi-single-helicity (QSH), an intermediate configuration with a single dominant mode but with secondary modes retaining residual non-negligible amplitudes. In all the RFP experiments, QSH is more frequently observed with larger plasma current and a weakly or non-reversed edge toroidal field [8]. The RFX-mod power supply capability [9] and advanced edge radial field feedback control [10] allow QSH characterization up to 2 MA of plasma current [11]. QSH are observed in the Madison Symmetric Torus (MST) [12] at a lower current than in RFX-mod [13–15]. This suggests that, perhaps, the smaller aspect ratio and the presence of a close-fitting shell facilitate QSH formation in MST.

In this work we attempt a reconstruction of the helical magnetic surfaces associated with the dominant mode, adapting to the MST configuration the force-free toroidal MHD model [16] developed for RFX-mod. In the first step, the model computes the axisymmetric equilibrium compatible with the edge magnetic measurements, upon optimizing a suitable parameterization of the current density radial profile. In the second step, the perturbations of this equilibrium are obtained solving a system of Newcomb-like equations formulated in toroidal geometry, using again the edge magnetic data as constraints. In the third step, the helical magnetic surfaces ensuing from the superposition of the axisymmetric equilibrium and the perturbation associated with the dominant mode are determined in the QSH states. The analysis focuses on non-reversed plasmas, where the equilibrium toroidal field is zero at the edge [15], since this condition guarantees the best QSH in terms of persistence and spectral purity. A slight generalization of the toroidal MHD model is necessary to provide a high-quality reconstruction. In fact the standard α–θ_0 parametrization for the current density [17] is not able to reproduce both the axisymmetric edge magnetic data and the resonance condition of the dominant mode in these discharges. A third parameter, suggested by the behavior at the plasma edge of the current density in the paramagnetic pinch equilibrium, is introduced. The ensuing reconstruction leaves some freedom in the location of the resonant surface of the dominant mode, which is partially solved by the inversion of the line-integrated electron density and the soft-x-ray (SXR) emissivity, considered constant on the helical surfaces. The good quality of such inversions validates the magnetic reconstruction.

This partial magnetic reconstruction is obtained ignoring the contribution of the secondary modes, but it describes fairly well the plasma core when the X-point of the magnetic island produced by the dominant mode annihilates the main magnetic axis, resulting in a single-helical-axis (SHAx) configuration where the island O-point becomes the new helical axis. In fact, SHAx is found to be more resilient to the magnetic chaos produced by the secondary modes. This configuration has been extensively studied in RFX-mod [18–20]. Poincarè plots based on RFX-mod magnetic data show how helical magnetic surfaces associated with the dominant mode, otherwise recognizable only in a small region around the resonant surface, appear in a significant portion of the plasma in SHAx states [19]. Consequently, the RFX-mod kinetic quantities can be considered constant on the SHAx helical surfaces [18, 20]. SHAx in RFX-mod occurs when the normalized amplitude of the dominant mode exceeds a threshold of about 4% [19]. A similar characterization has not been performed yet in MST, but we can say that the helical surfaces of the QSH examined in this work produce a SHAx configuration.

This is confirmed by the good inversion of the kinetic quantities mentioned above, indicating the existence of flux surfaces in a significant portion of plasma.

This work aims at further integration and sharing of analysis tools in the RFP community. The paper is organized as follows. Section 2 describes the MHD model used for the magnetic reconstruction. Section 3 discusses the means by which kinetic quantities are mapped onto helical magnetic surfaces. Section 4 is devoted to conclusions and final comments.

2. The MHD toroidal model

The MHD equilibrium model is described in detail in [16]. Here we provide a summary of the basic equations, and the adaptation necessary to the MST.

2.1. Basic equations

Each magnetic quantity is divided into a zeroth-order axisymmetric component and a perturbation term: $X(r, \vartheta, \phi) = X_0(r, \vartheta) + x(r, \vartheta, \phi)$. The coordinates $u^i \equiv (r, \vartheta, \phi)$ are defined by the zeroth-order magnetic surfaces, assumed to be non-concentric circles: r is their radius, ϑ is a poloidal-like angle referred to their centers, and ϕ is the geometrical toroidal angle. The model solves the linearized, ideal-MHD, zero-pressure force-balance equations

$$\boldsymbol{J}_0 \times \boldsymbol{B}_0 = 0 \Rightarrow \mu_0 \boldsymbol{J}_0 = \sigma \boldsymbol{B}_0 \tag{1}$$

$$\boldsymbol{J}_0 \times \boldsymbol{b} + \boldsymbol{j} \times \boldsymbol{B}_0 = 0 \tag{2}$$

coupling them with Ampere's law

$$\nabla \times \boldsymbol{B} = \mu_0 \boldsymbol{J} \tag{3}$$

and the divergence-free representation of the magnetic field in terms of two potentials, Ψ_t and Ψ_p:

$$\boldsymbol{B} = \nabla \Psi_t \times \nabla \vartheta - \nabla \Psi_p \times \nabla \phi. \tag{4}$$

In general the coordinates are not orthogonal, so we have to distinguish the contravariant components from the covariant components. The former are the projections along the gradients' basis:

$$B^r = \boldsymbol{B} \cdot \nabla r = b^r = -\frac{1}{\sqrt{g}} \left(\frac{\partial \Psi_t}{\partial \phi} + \frac{\partial \Psi_p}{\partial \vartheta} \right); \qquad B^\vartheta = \boldsymbol{B} \cdot \nabla \vartheta = \frac{1}{\sqrt{g}} \frac{\partial \Psi_p}{\partial r};$$

$$B^\phi = \boldsymbol{B} \cdot \nabla \phi = \frac{1}{\sqrt{g}} \frac{\partial \Psi_t}{\partial r} \tag{5}$$

where $1/\sqrt{g(r,\vartheta)} = \nabla r \times \nabla \vartheta \cdot \nabla \phi$ ($B_0^r = 0$ by definition). The latter are the projections $B_i = \boldsymbol{B} \cdot \boldsymbol{e}_i$ along the dual basis formed by the vectors $\boldsymbol{e}_i = \partial \boldsymbol{x}/\partial u^i$, where $\boldsymbol{x}$ is the position vector. The two kinds of component are related by $B_i = \sum_j B^j g_{ij}$, where $g_{ij} = \boldsymbol{e}_i \cdot \boldsymbol{e}_j$ is the metric tensor. The analytical treatment of the above equations is simplified by working in flux coordinates, defined by a proper choice of the poloidal-like angle, which makes Ψ_{t0} and Ψ_{p0} functions of r only. These two quantities become, respectively, the toroidal and the poloidal fluxes enclosed by the magnetic surface of radius r, divided by 2π. It is possible to show that even σ, defined by (1), becomes a function of r only, in the flux coordinate system. The zeroth-order equilibrium and the metric terms are then computed using a perturbative expansion in the inverse aspect ratio parameter a/R_0. The equilibrium is solved completely when the function $\sigma(r)$ and the boundary condition for the Shafranov shift are given. The latter is the displacement $\Delta(r)$ of the magnetic surface centers from the vacuum chamber

center. The Fourier harmonics $\psi_t^{m,n}$ and $\psi_p^{m,n}$ of the potential perturbations are defined by the expansion $x(r, \vartheta, \phi) = \sum_{m,n} x^{m,n}(r) e^{i(m\vartheta - n\phi)}$. For a given $n \neq 0$ they are the solutions of a system of infinite Newcomb-like equations, where the different m numbers are coupled by the $m = 1$, $n = 0$ harmonic of the metric terms (toroidal coupling). For practical evaluations, a suitable truncation of this system must be adopted. The ensuing reduced system is solved computing a basis of independent solutions, which must be combined to obtain the physical solution, with coefficients determined by the boundary conditions. The number of independent solutions is the sum of the number of poloidal harmonics considered (i.e. the number of equations) and the number of resonant harmonics. Upon defining the safety factor as $q(r) = (\mathrm{d}\Psi_{t0}/\mathrm{d}r)/(\mathrm{d}\Psi_{p0}/\mathrm{d}r)$, the m, n harmonic is resonant at $r = r^{m,n}$ if the condition $q(r^{m,n}) = m/n$ holds inside the plasma ($r^{m,n} < a$). The assumption of zero pressure within the model is justified by the relatively low β of the present RFP experiments ($\beta_\theta \approx 7\%$ in standard MST plasmas). Furthermore, the inclusion of this effect would increase considerably the complexity of the equations for the perturbations.

2.2. MST boundary conditions

The MST plasma is contained by a single conducting shell, with major radius $R_0 = 1.5$ m and minor radius $b = 0.52$ m, which also serves as the vacuum chamber and single-turn toroidal field winding. The plasma radius a is limited to $r_L = 0.51$ m by a toroidal graphite limiter on the inner surface of the shell. Since the MST pulse length (about 60 ms) is much shorter than the shell time constant (820 ms), the shell penetration of magnetic field lines can be safely discarded in our computation. In this case the shell inner surface coincides with the zeroth-order magnetic surface having $r = b$, which means that the Shafranov shift is zero there: $\Delta(b) = 0$. Likewise, one can assume a vanishing radial magnetic field produced by the tearing perturbation: $b^r(b) = 0$. According to (5) this condition translates into

$$m\psi_p^{m,n}(b) - n\psi_t^{m,n}(b) = 0 \qquad \forall m, n. \tag{6}$$

Constraint (6) can be invalidated by the presence of error fields. This point will be discussed in section 2.4. A toroidal array of pick-up coils, mounted on the inner surface of the shell at the poloidal position $\vartheta = \vartheta_{\mathrm{meas}}$, provides the toroidal B_ϕ^{meas} and poloidal $B_\vartheta^{\mathrm{meas}}$ magnetic fields at, respectively, 64 and 32 equally spaced toroidal angles [21, 22]. A different notation is used for the measured components, since they do not coincide with those of the flux-coordinate system. For the toroidal component we have $B_\phi^{\mathrm{meas}} = RB^\phi$, where $R(r, \vartheta)$ is the major radius. For the poloidal component, taking into account that the coils lie on the $r = b$ magnetic surface, one obtains $B_\vartheta^{\mathrm{meas}} = B_\vartheta/\sqrt{g_{\vartheta\vartheta}}$. The toroidal Fourier harmonics of these measurements provide two additional boundary conditions for the perturbation. In particular, using (5) and the property $R^2/\sqrt{g} = K(r)$, where $K(r)$ is a metric quantity given by R_0/r plus corrections order $(a/R_0)^2$ [16], one obtains

$$(B_\phi^{\mathrm{meas}})^n = \frac{K(b)}{R(b, \vartheta_{\mathrm{meas}})} \sum_m \frac{\mathrm{d}\psi_t^{m,n}(b)}{\mathrm{d}r} e^{im\vartheta_{\mathrm{meas}}}. \tag{7}$$

Concerning the poloidal field, we exploit the vacuum condition $j^r = 0$, which provides the relation

$$K(r)\frac{\partial^2 \Psi_t}{\partial\vartheta\,\partial r} - \frac{\partial B_\vartheta}{\partial\phi} = 0. \tag{8}$$

Making use of (8) and of the $B_\vartheta^{\mathrm{meas}}$ definition given above, one derives

$$(B_\vartheta^{\mathrm{meas}})^n = -\frac{K(b)}{\sqrt{g_{\vartheta\vartheta}(b, \vartheta_{\mathrm{meas}})}} \sum_m \frac{m}{n} \frac{\mathrm{d}\psi_t^{m,n}(b)}{\mathrm{d}r} e^{im\vartheta_{\mathrm{meas}}}. \tag{9}$$

Note that the $m = 0$ harmonic does not contribute to the poloidal field expansion (9).

2.3. Reconstruction of the zeroth-order equilibrium

The expression

$$\sigma(r) = \frac{2\theta_0}{a}\left[1 - \left(\frac{r}{a}\right)^\alpha\right]; \qquad \alpha > 1 \tag{10}$$

borrowed from the α–θ_0 model [17], which is standard in RFP cylindrical analysis, is a simple way to model a decreasing profile constrained by the symmetry requirement $\mathrm{d}\sigma(0)/\mathrm{d}r = 0$. The property $\sigma(a) = 0$ idealizes the condition that the current density is small at the plasma edge, though in general there are not physical reasons to impose the zeroing at $r = a$. In (10) the plasma radius is defined by $a = r_L - \Delta(a)$. Upon optimizing α and θ_0, the model should be able to fit the experimental pinch Θ and reversal F parameters, which characterize globally the RFP equilibrium. They are, respectively, the poloidally averaged edge poloidal and toroidal fields normalized by the poloidal-cross-section-average toroidal field. Non-reversed discharges have $F = 0$. Within the toroidal formalism these parameters can be expressed as

$$\Theta = \left(\oint \frac{g_{\vartheta\vartheta}(b,\vartheta)}{\sqrt{g(b,\vartheta)}}\,\mathrm{d}\vartheta\right)\frac{b}{4\pi}\frac{\Psi'_{p0}(b)}{\Psi_{t0}(b)}; \qquad F = K(b)\frac{b^2}{2R_0}\frac{\Psi'_{t0}(b)}{\Psi_{t0}(b)}; \qquad {}' \equiv \mathrm{d}/\mathrm{d}r. \tag{11}$$

This procedure is applied routinely in RFX-mod and provides satisfactory reconstructions of the zeroth-order equilibrium [18]. In contrast, the model (10) fails for the non-reversed MST discharges. It predicts $q(0) < 0.2$, whereas there are indications supporting the existence of the $m = 1$, $n = 5$ resonant mode in these discharges, which would necessarily imply $q(0) > 0.2$. First, the poloidal field Fourier analysis shows a substantial $n = 5$ harmonic, which can be identified as $m = 1$ since, according to (9), the $m = 0$ harmonic does not contribute to the vacuum poloidal field, and the $|m| > 1$ harmonics, if present, have smaller amplitudes. Second, the $m = 1$, $n = 5$ transition from the fast rotation at low amplitude to zero rotation at large amplitude is well reproduced by a model considering a resonant tearing mode interacting with the eddy current induced in the shell [15]. The $m = 1$, $n = 5$ amplitude growth also brings the plasma into the QSH condition in which the magnetic spectrum is dominated by this harmonic. A QSH example is given in figure 1 for the $F = 0$ discharge 1090604127.

The inadequacy of the force-free α–θ_0 model for the $F = 0$ discharges has been already encountered in previous cylindrical analysis [15]. In this geometry, keeping expression (10) and including pressure with $\beta_\theta = 7\%$ in the equilibrium equations, the $m = 1$, $n = 5$ mode can be made resonant [15]. However, the addition of pressure does not seem a feasible strategy in the framework of the toroidal model, since an unrealistic $\beta_\theta > 20\%$ would be necessary for matching the experimental Θ, $F = 0$, and the condition $q(0) > 0.2$. In contrast, these requirements can be satisfied maintaining the force-free assumption with a more suitable model for $\sigma(r)$. This is suggested by the paramagnetic pinch Ohm's law

$$\boldsymbol{E}_0 + \boldsymbol{V}_0 \times \boldsymbol{B}_0 = \eta\boldsymbol{J}_0 \tag{12}$$

applied to the $F = 0$ equilibrium. Equation (12) is valid inside the plasma, namely for $r \leqslant a$, and $\boldsymbol{E}_0$, $\boldsymbol{V}_0$, η are, respectively, the zeroth-order electric field, fluid velocity and plasma resistivity. The electric field satisfies the stationary condition $\nabla \times \boldsymbol{E}_0 = 0$ and can therefore be written as

$$\boldsymbol{E}_0 = V_\phi \nabla\phi + \nabla\varphi_0(r,\vartheta) \tag{13}$$

where the constant V_ϕ is the toroidal loop voltage, and φ_0 is the electrostatic potential. Equations (12) and (13) do not apply to the RFP equilibrium due to the additional electric field produced by the dynamo process. Although the dynamo is likely to be active also in the $F = 0$ case, we will examine the two equations all the same, since they indicate a possible way
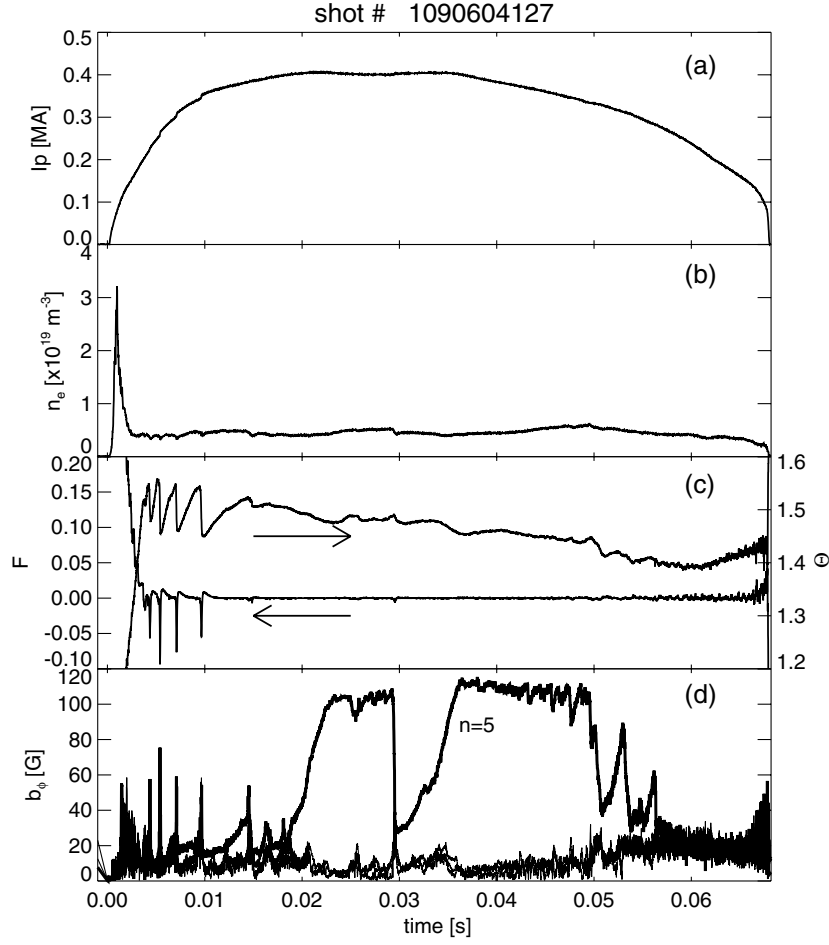
Figure 1. Waveforms of a *non-reversed* discharge 1090604127. (*a*) Plasma current, (*b*) electron density, (*c*) reversal and pinch parameters, (*d*) toroidal field harmonics $(B_\phi^{\text{meas}})^n$ for the dominant $n = 5$ perturbation (thick line) and some of the secondary modes ($n = 6, 7, 8$).

to improve the α–θ_0 model for the $F = 0$ discharges. Using (1) and (13), the scalar product of (12) with B_0 gives

$$V_\phi B_0^\phi + \frac{\partial \varphi_0}{\partial \vartheta} B_0^\vartheta = \frac{\eta}{\mu_0} \sigma B_0^2. \tag{14}$$

Exploiting (5) and the poloidal average $\langle f \rangle = \oint d\vartheta \sqrt{g} f / (2\pi)$ one obtains

$$\sigma(r) = \mu_0 V_\phi \frac{\Psi_{t0}'}{\langle \eta B_0^2 \rangle}. \tag{15}$$

Making use of the force-balance equation $d(K \Psi_{t0}')/dr = -\sigma \Psi_{p0}'$, which derives from (1), (3), (5) as shown in [16], we also find that

$$\frac{d\sigma}{dr} = -\mu_0 V_\phi \frac{\mu_0 V_\phi \Psi_{p0}' + \frac{d}{dr}(K \langle \eta B_0^2 \rangle)}{K \langle \eta B_0^2 \rangle^2} \Psi_{t0}'. \tag{16}$$

The condition $\Psi_{t0}' = 0$ holds in the entire vacuum region $a \leqslant r \leqslant b$ in $F = 0$ discharges, due to the definition in (11) and to the above-mentioned force-balance equation ($\sigma = 0$ in vacuum).
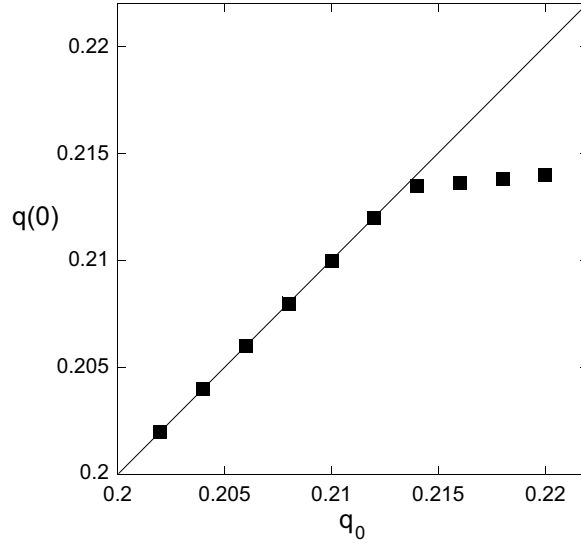
Figure 2. Comparison between the targeted q_0 and the computed on-axis value $q(0)$ of the safety factor. The model (18) is adopted. The experimental data come from the shot 1090604127 at $t = 27$ ms.

From $\Psi'_{t0}(a) = 0$ and (15), (16) we obtain the two constraints $\sigma(a) = 0$ and $d\sigma(a)/dr = 0$, regardless of the resistivity profile. The α–θ_0 model satisfies the first, but violates the second. Therefore, seeking for a more appropriate model of the $F = 0$ equilibrium, we can also require that $d\sigma/dr = 0$ both at $r = 0$ and $r = a$:

$$\frac{d\sigma}{dr} \propto \left(\frac{r}{a}\right)^{\alpha} \left[1 - \left(\frac{r}{a}\right)^{\gamma}\right]; \qquad \alpha > 0, \quad \gamma > 0. \tag{17}$$

The condition $\gamma > 0$ ensures regularity at $r = 0$. The additional constraint $\sigma(a) = 0$ provides

$$\sigma(r) = \frac{2\theta_0}{a} \left[1 + \frac{\alpha + 1}{\gamma} \left(\frac{r}{a}\right)^{\alpha+\gamma+1} - \frac{\alpha + \gamma + 1}{\gamma} \left(\frac{r}{a}\right)^{\alpha+1}\right]. \tag{18}$$

The definition $\sigma(0) = 2\theta_0/a$ has been maintained, and the α–θ_0 expression is recovered in the limit of large γ. The model (18) allows matching of the experimental Θ and $F = 0$, and the condition $q(0) > 0.2$ by a proper optimization of the free parameters α, γ and θ_0. An example of such an equilibrium reconstruction is shown in figures 2–5 for the same $F = 0$ discharge as in figure 1, at $t = 27$ ms. Since $q(0)$ is not measured, different targeted on-axis values $q_0 > 0.2$ are tried. Therefore, the optimization tries to match the parameters Θ, $F = 0$ and q_0. As shown in figure 2, q_0 may be different from the ensuing $q(0)$ of the optimized equilibrium. There is a range of possible equilibrium profiles, obtained up to $q_0 = 0.212$, which reproduce the experimental Θ, F and the condition $q(0) > 0.2$. Moreover, $q(0) = q_0$ for these good profiles. In contrast, for $q_0 > 0.212$ the model is not able to match exactly the experimental Θ and F. The solutions obtained with $q_0 = 0.202$ ($\theta_0 = 1.626$, $\alpha = 2.535$, $\gamma = 35.228$) and $q_0 = 0.212$ ($\theta_0 = 1.551$, $\alpha = 4.910$, $\gamma = 6.025$) are compared in figure 5. Note that as $q(0)$ increases above 0.2 the equilibrium departs from the α–θ_0 model, i.e. γ decreases. Differences in $\sigma(r)$ do not have a significant impact on the global magnetic field profile.

Nonetheless, the $m = 1$, $n = 5$ resonant surface location is sensitive to small equilibrium variations, since one finds that $r^{1,5} = 0.0458$ m for $q_0 = 0.202$ and $r^{1,5} = 0.1136$ m for $q_0 = 0.212$. The possibility of providing further constraints on the possible equilibria is
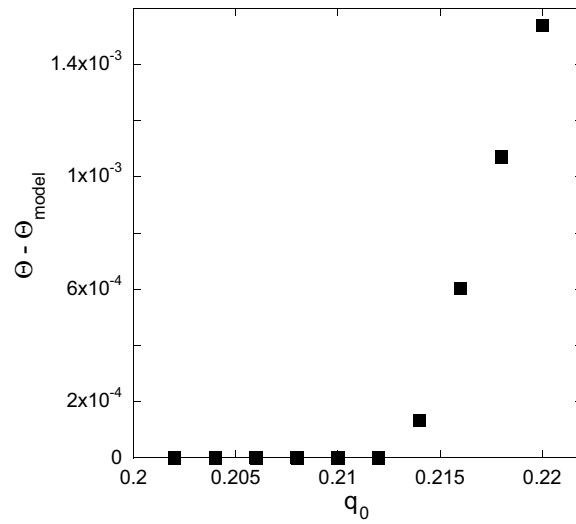
Figure 3. Difference between the experimental Θ and computed Θ_{model} pinch parameter for the same analysis considered in figure 2.
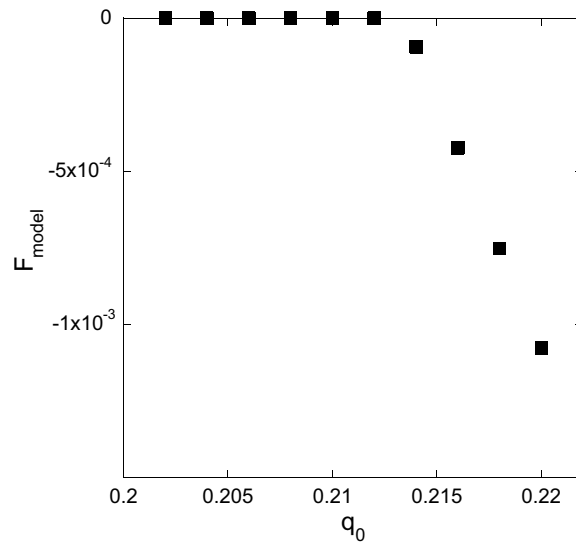

Figure 4. Computed F_{model} reversal parameter for the same analysis considered in figure 2, to be compared with the experimental value $F = 0$.

discussed in section 3. We note that it is not guaranteed for any three parameters modeling $\sigma(r)$ to reproduce the experimental Θ, $F = 0$, and the condition $q(0) > 0.2$. For example, the expression

$$\sigma(r) = \frac{2\theta_0}{a} \left[1 - \left(\frac{r}{a} \right)^{\alpha} \right] \cdot \left[1 + \gamma \left(\frac{r}{a} \right)^{2} \right],$$

where the second bracketed term allows for a concavity in the profile, does not work. In contrast, the α–θ_0 model (10) with two different exponents, namely $\alpha = \alpha_1$ for $r < a/2$ and
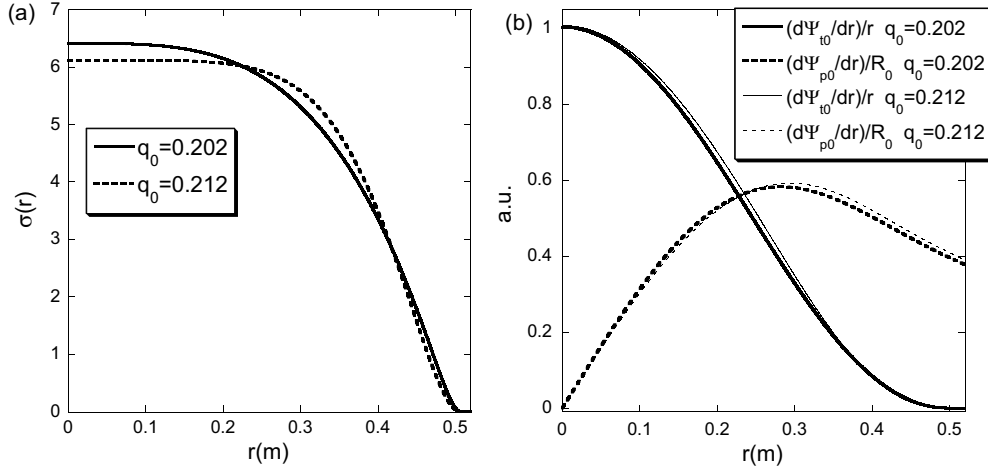
Figure 5. Two examples of equilibrium profiles compatible with the experimental condition for the analysis reported in figure 2. The abscissa extends to the shell radius. (*a*) $\sigma(r)$ profile, (*b*) radial derivatives of the normalized zeroth-order fluxes Ψ_{t0}, Ψ_{p0}, divided by factors which give them the shape of toroidal and poloidal magnetic fields, respectively.

$\alpha = \alpha_2$ for $a/2 \leqslant r \leqslant a$ can work up to the targeted value $q_0 = 0.208$. Nonetheless, the profile given by (18) has the advantage of being smooth and somewhat better justified. Therefore, it will be adopted by the following analysis.

2.4. Reconstruction of the $n = 5$ perturbation

The largest-amplitude perturbations in MST are the $m = 1$ resonant harmonics corresponding to the dynamo tearing modes. They typically have $n \geqslant 5$ in $F = 0$ discharges. When considering the $n = 5$ perturbation, which becomes dominant in these discharges, we can limit the system of Newcomb-like equations to the $m = 0$, 1, and 2 poloidal harmonics. The same truncation applies to the summations in the boundary conditions (7) and (9). The $m = 0$ corresponds to a resonant tearing mode only for $F < 0$. For $F = 0$, both $m = 0, n = 5$ and $m = 2, n = 5$ are non-resonant harmonics, which, in the absence of external sources such as error fields, are pure toroidally generated sidebands of the $m = 1$ (the $m = 0$ modes also derive from the nonlinear $m = 1$ coupling, but this effect is not considered in the present model). Therefore, the number of independent solutions is four. The ideal-shell constraint (6) and the two measurements (7) and (9) provide a redundant condition. It is reasonable to retain both (7) and (9), since they come from a measurement, whereas one can drop one of the ideal-shell constraints for a specific poloidal number $m = \bar{m}$. In general, this determines a multi-harmonic error field with a main component $(b^r)^{\bar{m},n}(b) \neq 0$, and secondary toroidally coupled harmonics $(b^r)^{\bar{m}\pm 1,n}(b) \neq 0$ produced by the factor $1/\sqrt{g(r, \vartheta)}$ in the first equation in (5). On the other hand, radial magnetic error fields occur both at the toroidal and poloidal gaps (the horizontal and vertical insulated cuts in MST's conducting shell) with a fairly broad m and n spectrum [15, 22].

The reconstruction of the $n = 5$ perturbation for the same shot and time considered in figures 2–5, where the related $m = 1$ mode becomes dominant, is now discussed. Taking $\bar{m} = 2$, the computed b^r radial profile is unrealistic, having too large an amplitude at the shell (see figure 6). The profile becomes more reasonable with $\bar{m} = 1$ (see figure 7), but the smallest
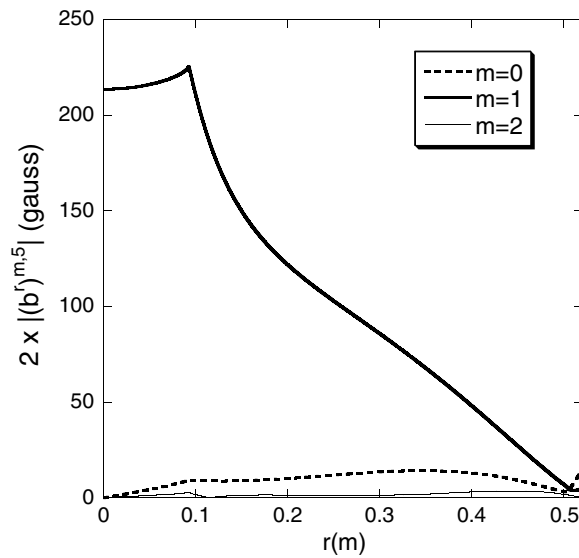
9
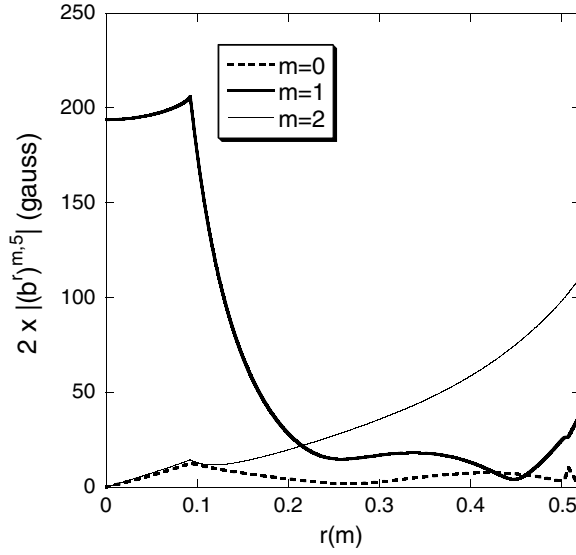
Figure 6. Amplitudes of the harmonics $(b^r)^{m,5}(r)$ for the shot 1090604127 at $t = 27$ ms. The underlying zeroth-order equilibrium refers to the case $q_0 = 0.208$. The estimate discards the condition (6) for the $m = 2$ harmonic. Note that even $(b^r)^{1,5}(b) \neq 0$ due to the toroidal coupling with $m = 2$. The factor 2 in the amplitude takes into account the complex conjugate harmonic contribution. The abscissa extends to the shell radius. Note the unrealistically large value of the perturbation there.
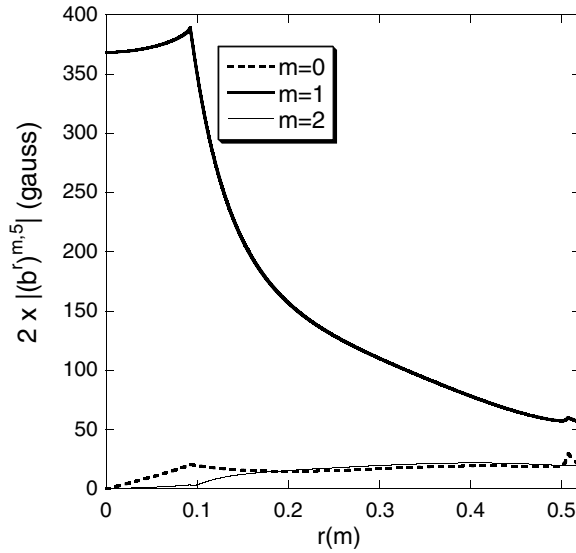

Figure 7. Same quantity considered in figure 6. The underlying zeroth-order equilibrium refers to the case $q_0 = 0.208$. The computation discards the condition (6) for the $m = 1$ harmonic. The perturbation at the shell radius remains quite large.

error field amplitude is obtained for $\bar{m} = 0$ (see figure 8). The latter will be maintained in the following. If one takes $\bar{m} = 1$, the maximum b^r amplitude inside the plasma would be sensitive to the choice of the zeroth-order equilibrium, showing a very irregular dependence on q_0 in the interval $0.202 \leqslant q_0 \leqslant 0.212$. Instead, with $\bar{m} = 0$ the amplitude dependence on

Figure 8. Same quantity considered in figure 6. The underlying zeroth-order equilibrium refers to the case $q_0 = 0.208$. The computation discards the condition (6) for the $m = 0$ harmonic. Now the perturbation amplitude at the edge is reasonable and compatible with the presence of a small-error field.
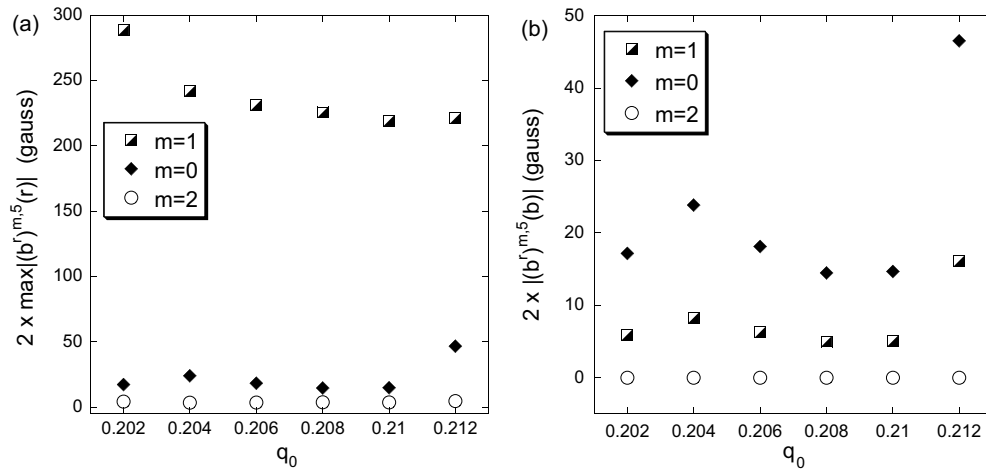
Figure 9. Maximum (*a*), and edge (*b*) amplitudes of the harmonics $(b^r)^{m,5}(r)$ in the shot 1090604127 at $t = 27$ ms, obtained for the equilibria ($0.202 \leqslant q_0 \leqslant 0.212$), which according to figures 2–4 satisfy the global experimental requirements. The estimate discards the condition (6) for the $m = 0$ harmonic. The factor 2 takes into account the complex conjugate harmonic contribution

q_0 is weak, as figure 9(*a*)) clearly shows. This fact gives us confidence in the robustness of the reconstruction obtained with $\bar{m} = 0$. However, this assumption remains an approximation. A less approximate reconstruction would require an extensive set of edge b^r measurements, which would then be used in place of the ideal-shell condition (6). Concerning this point, MST is equipped with measurements of the error field and its poloidal spectrum at the poloidal

gap [15], but it is not possible to include these data in the reconstruction, lacking a resolution in the toroidal mode number n. Moreover, even the toroidal gap and the portholes are sources of errors, for which measurements are not routinely available. However, at least the order of magnitude of the error field estimated by the reconstruction should be correct. Let us consider in figure 9(*b*)) the error field amplitude dependence on the possible zeroth-order equilibrium. Apart from the case $q_0 = 0.212$, which is rejected owing to the very large $b^r(b)$, the $m = 1$ component has an amplitude below $10\,\mathrm{G}$, which is compatible with the measurement at the poloidal gap in the so-called 'small-error' discharges in figure 6 of [15].

Finally, we have also tried the reconstruction using the standard α–θ_0 model, which renders the $m = 1, n = 5$ mode non-resonant. In this case the number of independent solutions is three, and the measurements (7) and (9) must be complemented by one of (6). Taking (6) for $m = 0$ gives unrealistic profiles, whereas reasonable results are obtained imposing the condition (6) for $m = 1$ or $m = 2$. However, the estimated error field increases with respect to the previous reconstruction: the RMS of the harmonics $(b^r)^{m=0,1,2,\,n=5}(b)$ is about $14.5\,\mathrm{G}$ compared with $8.8\,\mathrm{G}$ obtained with the profiles of figure 8. The α–θ_0 model based reconstruction will be discussed again in section 3.2.

2.5. Helical surfaces of the dominant mode

Let us approximate the QSH magnetic structure as the superposition of the zeroth-order axisymmetric equilibrium and the perturbation due only to the dominant m, n mode ($m = 1$, $n = 5$ in our case):

$$\Psi_\mathrm{p}(r, u) = \Psi_\mathrm{p0}(r) + \psi_\mathrm{p}^{m,n}(r)\mathrm{e}^{\mathrm{i}u} + \text{c.c.} \qquad \Psi_\mathrm{t}(r, u) = \Psi_\mathrm{t0}(r) + \psi_\mathrm{t}^{m,n}(r)\mathrm{e}^{\mathrm{i}u} + \text{c.c.} \qquad (19)$$

Here $u = m\vartheta - n\phi$ is the helical angle. From (4) and (19) it is straightforward to show that the combination $\chi(r, u) = m\Psi_\mathrm{p}(r, u) - n\Psi_\mathrm{t}(r, u)$ is a flux function: $\boldsymbol{B} \cdot \nabla\chi = 0$. Thus, in this approximation, helical magnetic surfaces, identified by constant helical flux χ, do exist. The SHEq code, developed for RFX-mod [20], has been interfaced with the MST adaptation of the toroidal MHD model, and it is able to display the shape of the magnetic surfaces in the machine coordinate system. In particular, it manages the transformation between the machine and flux coordinates used by the toroidal model. The final passage to the machine coordinates is necessary if we want to cross-check the magnetic reconstruction with other diagnostics. As mentioned in the introduction, when adding the secondary modes, the helical magnetic surfaces should survive in a significant region of the plasma in only the SHAx state. The latter is recognized by the monotonic behavior of χ: each value of χ corresponds to just one surface. With this condition it is useful to define the effective radius by

$$\rho = \sqrt{\frac{\chi - \chi_0}{\chi_\mathrm{a} - \chi_0}} \qquad (20)$$

where χ_0 is the helical flux on the helical magnetic axis, and χ_a is the helical flux of the plasma boundary. The variable ρ ranges between 0 (on the helical axis) and 1.

3. Comparison with the kinetic measurements

The mapping of certain kinetic quantities onto the MST reconstructed helical flux surfaces is now discussed. This effort parallels the successful effort in SHAx analysis in RFX-mod [18]. Due to fast parallel transport of electrons and electron energy, both plasma electron density and temperature can be handled as flux functions. Consequently, this is also true for the SXR bremsstrahlung. Electron density and SXR emission are considered in the present analysis.
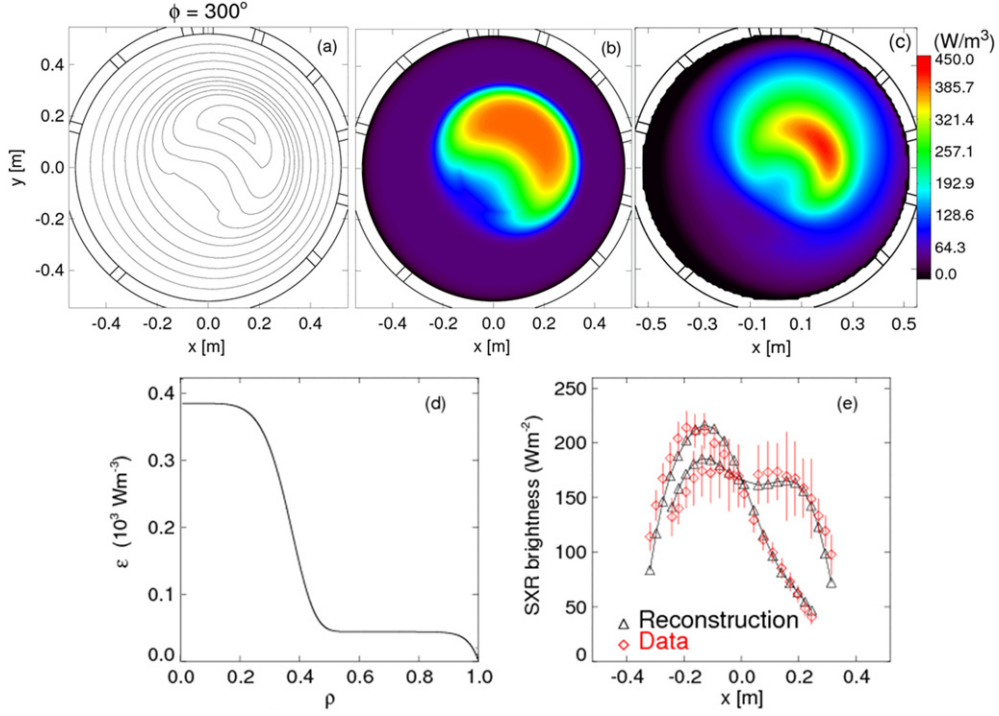
Figure 10. Mapping of the SXR emissivity onto the helical flux surfaces of the SHAx observed at $t = 26$ ms in the shot 1100915079. (*a*) Reconstruction of the flux surfaces at the diagnostic toroidal section. (*b*) 2D map of the emissivity as a flux function; the best fit inversion parameters, according to equation (22), are $\varepsilon_{glob} = 44$ W m^{-3}, $\varepsilon_1 = 18$, $\varepsilon_{int} = 341$ W m^{-3}, $\varepsilon_2 = 0.4$, $\varepsilon_3 = 6$. (*c*) 2D map of the emissivity as obtained from the measurements with the Bessel–Cormack technique. (*d*) Emissivity profile as a function of the effective radius across the helical structure. (*e*) Comparison between the experimental brightness (integrated emissivity), and those computed along the 40 lines of sight of the two-camera SXR diagnostic using the map shown in (*b*); the abscissa is the chord impact parameter with the usual sign convention.

The dependence of these quantities on the effective radius ρ is modeled leaving some free parameters, which are optimized upon minimizing the discrepancy

$$\chi^2 = \sum_i \frac{(f_i - f_{i,\text{model}})^2}{\sigma_i^2} \tag{21}$$

between the measurements f_i and their numerical model-based reconstruction $f_{i,\text{model}}$. The measurement errors σ_i are taken into account. If the geometry of the flux surfaces is correct, good agreement is expected, whereas numerical and experimental data will not match when the magnetic pattern has an incorrect shape.

3.1. SXR emissivity

The SXR tomographic diagnostic [23] as applied in this analysis has a total of 40 lines of sight divided between two cameras viewing the plasma at the same toroidal position ($\phi_{\text{SXR}} = 300°$) but from two different ports. Tomographic data from an $F = 0$, $I_{\text{p}} = 500$ kA discharge is shown in figure 10. A discharge with this current and electron temperature ensures adequate SXR emission for the diagnostic. The measurements f_i are the emissivities integrated along

the chords (SXR brightness), and the sum (21) is calculated over all the lines of sight of the diagnostic. SXR emissivity ε is modeled with the following flux function:

$$\varepsilon(\rho) = \varepsilon_{\text{glob}}(1 - \rho^{\varepsilon_1}) + \varepsilon_{\text{int}} \exp\left[-\left(\frac{\rho}{\varepsilon_2}\right)^{\varepsilon_3} \right] \tag{22}$$

where $\varepsilon_{\text{glob}}$, ε_{int}, ε_1, ε_2, ε_3 are free parameters. The first term represents the global emissivity, while the exponential term is introduced to allow for an enhancement localized around the most internal surfaces. The analysis is performed at 26 ms where the $m = 1$, $n = 5$ SHAx is observed. Figure 10(*a*) displays the flux surfaces' poloidal cross section at the toroidal location of the SXR diagnostic. Note the bean-shaped central helical core, located in the upper outboard region of the vacuum chamber, surrounded by a nearly axisymmetric boundary. Figure 10(*b*) shows the poloidal 2D map of the SXR emissivity which emerges on these surfaces with the model (22) after the optimization of the free parameters. In figure 10(*c*), the same quantity computed with the usual Bessel–Cormack inversion of the measurements [24, 25] is presented. The emissivity regions of plots (*b*) and (*c*) agree reasonably well in radial and poloidal extent, and in both cases a high-emissivity helical core is surrounded by a nearly circular low-emissivity boundary. Figure 10(*d*) displays the emissivity profile $\varepsilon(\rho)$ derived from the model (22): the result is qualitatively similar to what is obtained in RFX-mod (see figure 4(*a*) of [18]). Figure 10(*e*) compares measured line-integrated emission data from each of the two SXR cameras with that based on the helical-surface-modeled brightness. The available magnetic constraints leave a certain degree of freedom for the internal reconstruction, mainly in the radial location of the $m = 1$, $n = 5$ resonant surface, as explained in section 2. The SXR analysis provides a means of selecting among the possible profiles. The worst discrepancy, $\chi^2 = 46.73$, corresponds to the most internal resonance ($r^{1,5} = 0.133$ m), whereas the best agreement, $\chi^2 = 27.81$, is obtained with the most external resonance ($r^{1,5} = 0.171$ m). The latter refers to the inversion shown in figure 10. The Bessel–Cormack inversion considered in panel (*c*) produces a further smaller discrepancy, $\chi^2 = 9.36$, but at the price of optimizing 35 independent variables against the five free parameters of the model (22). Since the evident difference between the two methods is not the resulting χ^2, but the number of free parameters, we draw the conclusion that the flux surfaces underlying the model (22) are reconstructed fairly well. It is true that the location of the most internal surfaces as shown in the map 10(*a*) is slightly upper shifted with respect to the most emissivity region of panel 10(*c*), but this is due to the respective errors of the two reconstructions: the MHD one is affected by the approximations due to the lacking of an adequate set of edge probes as explained in section 2.4, and even the Bessel–Cormack inversion does not perfectly match the measurements (χ^2 is not zero).

3.2. Electron density

A similar approach has been used to analyze the interferometric data. MST is equipped with a FIR interferometer/polarimeter diagnostic having 11 vertical chords arranged in two adjacent toroidal sections: five at $\phi = 250°$ and six at $\phi = 255°$ [26]. In this case the measurements f_i are the line-integrated densities along the chords. As with the SXR data, the density profile has been mapped over the helical flux surfaces, and the line-integrated densities have been computed for each set of chords. We have accounted for the fact that the poloidal location of the $n = 5$ helical structure differs by 25° between the two toroidal sections. The parameterization chosen for the density is

$$n_{\text{e}}(\rho) = (n_{\text{core}} - n_{\text{edge}})(1 - \rho^{n_1})^{n_2} + n_{\text{edge}}(1 - \rho^{n_3}) \tag{23}$$

where n_{core}, n_{edge}, n_1, n_2, n_3 are free parameters. The exponent n_3 determines the slope in the edge region, where significant modifications can be produced by this parameter. Examples
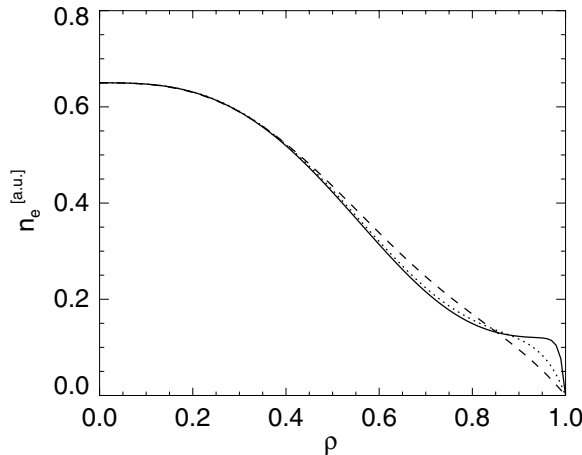
Figure 11. Density profiles according to parameterization (23), for three values of n_3. Continuous line refers to $n_3 = 100$; dotted line to $n_3 = 20$ and dashed line to $n_3 = 5$. The main differences take place in the outer portion of the profile, but do not significantly modify the inversion results.

of such variations are given in figure 11. The inversion result shows a weak but systematic dependence on n_3, passing from $\chi^2 = 13$ when $n_3 = 100$ (the best case) to $\chi^2 = 14$ when $n_3 = 5$. A detailed investigation of the edge density profile and its effects on particle transport is beyond the scope of this paper. Hence, we fix $n_3 = 100$, reducing the number of free parameters to four.

The result of the inversion over helical flux surfaces is compared with a 1D axisymmetric inversion code applied routinely to MST density data. The 1D code adopts the parameterization (23) but assumes that density is constant on non-concentric circular surfaces whose horizontal displacement δ is optimized within the procedure. We note that the 1D inversion does not involve any sort of magnetic reconstruction, so these circular surfaces are not necessarily aligned with magnetic flux surfaces. The displacement δ is modeled by $\delta(r) = \delta_0[1 - (r/a)^\lambda]$, where r is the surface radius. This code is appropriate when the density profile is determined mainly by the axisymmetric Shafranov-shifted equilibrium, as is the case in MH states. The fit parameter λ always falls very close to 3, so we fix $\lambda = 3$ in order to reduce computational complexity. This leaves five free parameters n_{core}, n_{edge}, n_1, n_2, δ_0 in the 1D code.

Figure 12 displays a $m = 1$, $n = 5$ SHAx with the helical structure located inboard at the interferometer toroidal angles. Plots (a)–(c) refer to the helical flux surface inversion, whereas plots (d)–(e) present the 1D code result. Qualitatively, both methods provide inward displacements of the plasma (see panels (a) and (d)). In particular the 1D code predicts $\delta_0 = -1$ cm, whereas the axisymmetric Shafranov shift is always positive. This indicates that the density profile is sensitive to the magnetic surface distortion induced by the dominant mode. This behavior is well described by the inversion over the helical flux surfaces, since the ensuing χ^2 is one fourth of that obtained by the 1D code. This confirms once more the existence of helical magnetic surfaces associated with the dominant mode inside the plasma as well as the reliability of their MHD reconstruction. The density inversion allows one to distinguish among the possible magnetic internal reconstructions. The optimum resonant surface location is found at $r^{1,5} = 0.103$ m, corresponding to $\chi^2 = 13.05$, whereas at the two extremes of the interval one finds $r^{1,5} = 0.046$ m with $\chi^2 = 18.53$ and $r^{1,5} = 0.123$ m with $\chi^2 = 13.57$. Figure 12 refers to the best inversion.
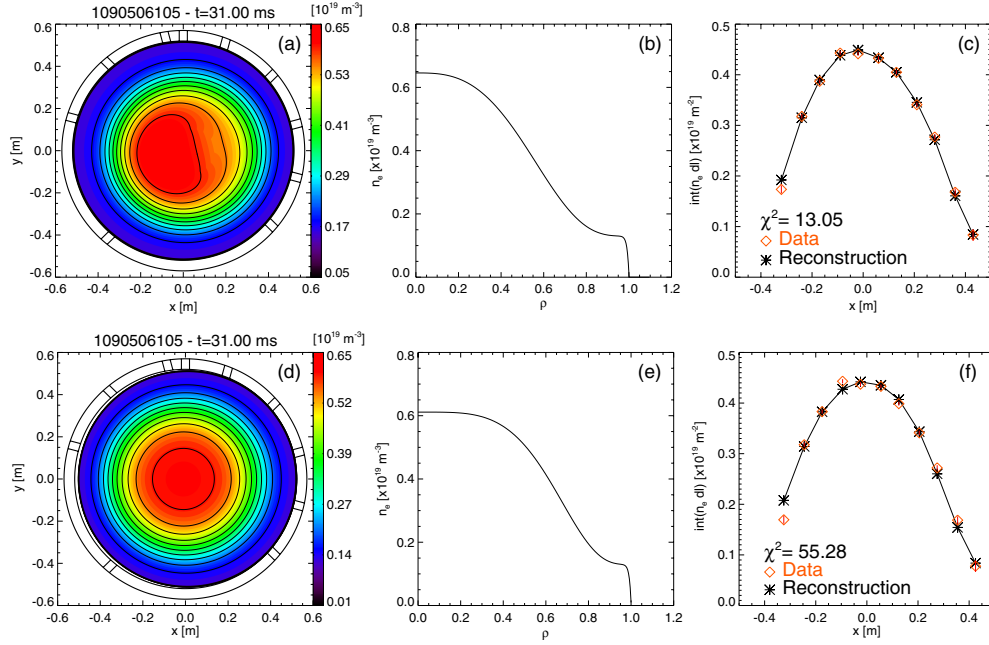
Figure 12. Density analysis for the SHAx observed at $t = 31$ ms in the shot 1090506105. (*a*) Electron density 2D mapping over the reconstructed helical flux surfaces at $\phi = 250°$. (*b*) Ensuing profile according to the model (23). (*c*) Comparison between numerical and experimental line integral density; the abscissa is the chord impact parameter with the usual sign convention. (*d*), (*e*), (*f*) show the same quantities provided by the 1D inversion code. The χ^2 comparison confirms that the density inversion over the helical flux surfaces is more accurate.

At the end of section 2.4, we mentioned the possibility of performing a magnetic reconstruction based on the α–θ_0 model, which requires the $m = 1$, $n = 5$ mode to be non-resonant, at the price of increasing the error field amplitude. The ensuing helical surfaces do not fit the density data as well as the previous reconstruction, since $\chi^2 = 25.22$ is obtained. This is another justification for using the model (18) to make the $m = 1$, $n = 5$ mode resonant.

4. Conclusions

A force-free method to reconstruct the magnetic field inside the MST plasma in a realistic toroidal geometry has been presented. This is based on models applied routinely in RFX-mod data analysis. The adaptation to the $F = 0$ MST discharges is not straightforward, since a generalization of the standard α–θ_0 model for the parallel current profile is necessary to match the global equilibrium. Since the new model has three parameters to optimize, whereas the two experimental constraints F and Θ are complemented only by the condition $q(0) > 1/5$, which makes the $m = 1$, $n = 5$ mode resonant, the reconstruction allows an ensemble of possible profiles. Likewise, the edge measurements are not sufficient for solving the system of equations describing the perturbations, and they must be supplemented by a 'relaxed ideal-shell' condition, compatible with the presence of a small-error field with a main $m = 0$ component. The dominant mode's helical flux surfaces reconstructed in $m = 1$, $n = 5$ QSH have been used to invert the electron density and SXR emissivity line-integrated measurements. In the cases discussed here the magnetic pattern exhibits a SHAx feature. Among the magnetic

profiles compatible with the external constraints, in the cases examined thus far both inversions help to identify the best reconstruction. The highest-quality inversions so obtained indicate the presence of magnetic helical surfaces in a significant portion of the plasma and provide an important benchmark for the magnetic reconstruction. Work is also underway to probe directly the helical magnetic topology using internal polarimetric techniques.

Euratom © 2011.

References

[1] Ortolani S and Schnack D D 1993 *Magnetohydrodynamics of Plasma Relaxation* (Singapore: World Scientific)

[2] Cappello S, Bonfiglio D and Escande D F 2006 *Phys. Plasmas* **13** 056102

[3] Ding W X, Brower D L, Craig D, Deng B H, Fiksel G, Mirnov V, Prager S C, Sarff J S and Svidzinski V 2004 *Phys. Rev. Lett.* **93** 045002

[4] Furth H P, Killen J and Rosenbluth M N 1963 *Phys. Fluids* **6** 459

[5] Arcis N, Escande D F and Ottaviani M 2007 *Phys. Plasmas* **14** 032308-1

[6] Merlin D, Ortolani S, Paccagnella R and Scapin M 1989 *Nucl. Fusion* **29** 1153

[7] Cappello S and Paccagnella R 1992 *Phys. Fluids* B **4** 611

[8] Martin P *et al* 2003 *Nucl. Fusion* **43** 1855

[9] Sonato P *et al* 2003 *Fusion Eng. Des.* **66** 161

[10] Zanca P, Marrelli L, Manduchi G and Marchiori G 2007 *Nucl. Fusion* **47** 1425

[11] Martin P *et al* 2010 *Overview of RFX fusion science program* OV/5-3Ra *23rd IAEA Fusion Energy Conf. (Daejeon, Republic of Korea, 11–16 October 2010) Nucl. Fusion.* submitted http://www-pub.iaea.org/ mtcd/Meetings/PDFplus/2010/cn180/cn180_papers/ov_5-3ra.pdf

[12] Dexter R N *et al* 1991 *Fusion Technol.* **19** 131

[13] Franz P *et al* 2006 *Phys. Plasmas* **13** 012510

[14] Marrelli L *et al* 2002 *Phys. Plasmas* **9** 2868

[15] Chapman B E, Fitzpatrick R, Craig D, Martin P and Spizzo G 2004 *Phys. Plasmas* **11** 2156

[16] Zanca P and Terranova D 2004 *Plasma Phys. Control. Fusion* **46** 1115

[17] Antoni V, Merlin D, Ortolani S and Paccagnella R 1986 *Nucl. Fusion* **26** 1711

[18] Lorenzini R *et al* 2009 *Nature Phys. Lett.* **5** 570

[19] Lorenzini R *et al* 2008 *Phys. Rev. Lett.* **101** 025005

[20] Martines E *et al* 2011 *Plasma Phys. Control. Fusion* **53** 035015

[21] Craig D 2005 Magnetic mode analysis in MST *MST Internal Document*

[22] Chapman J T 1998 Spectroscopic measurements of the MHD dynamo in the MST reversed field pinch *PhD Thesis* University of Wisconsin–Madison

[23] Franz P *et al* 2004 *Rev. Sci. Instrum.* **75** 4013

[24] Cormack A M 1964 *J. Appl. Phys.* **35** 2908

[25] Nagayama Y 1987 *J. Appl. Phys.* **62** 2702

[26] Burns S R, Peebles W A, Holly D and Lovell T 1992 *Rev. Sci. Instrum.* **63** 4993